Journal of Innovation and Development
ISSN: 2958-4752 | Vol. 15, No. 1, 2026

Spatiotemporal Evolution Characteristics of Stress Transfer in the Stress Concentration Zone at the Working Face End of Steeply Dipping Coal Seams

Zhonghua Xu

Henan polytechnic university, Jiaozuo, Henan, 454000, China

Abstract: Steeply dipping coal seams exhibit unique stress environments with spatiotemporal stress transfer in the stress concentration zone of the working face. Revealing these characteristics is crucial for safe and efficient mining. We investigated the spatiotemporal evolution of stress transfer in the stress concentration zone at the junction between the working face and the upper and lower roadways for the steeply dipping fully mechanized coal mining face (35050) of Yiluo Coal Mine. Field measurements and laboratory-determined mechanical properties of rock samples were used to analyze stress transfer paths at the working face end. During the working face advancements, the deformation of the overburden at the junction showed a greater displacement at the upper end than at the lower end. The structural evolution of the surrounding rock along the strike direction exhibited a periodic "stable–deformation–fracture–stable" pattern. Mining-induced stress showed asymmetric dip-ward and symmetric strike-ward transfer and evolution during working face advance. As the face advanced, the extent of the stress boundary line gradually increased. In the coal seam-parallel section, the stress boundary lines of the goaf and roof exhibited asymmetric arch-shaped distributions. The lower-end stress arch was significantly greater than the upper.

Keywords: Steeply Dipping Coal Seam; Stress Concentration Zone; Numerical Simulation; Spatiotemporal Evolution of Stress Transfer.

1. Introduction

Steeply dipping coal seams are widely distributed in major mining regions across China, with proven reserves ranging from 180 billion tons to 360 billion tons and an annual production of approximately 150 million tons to 300 million tons, accounting for 10% to 20% and 5% to 8% of the national coal reserves and production, respectively [1, 2]. Extensive engineering practices have demonstrated that after the extraction of steeply dipping coal seams, the deformation, damage, and movement patterns of the surrounding rock in the stope differ significantly from those observed in general coal seams [3]. Influenced by the dip angle and mining length of the coal seam, the stope surrounding rock structure formed during the mining process exhibits distinct characteristics. Given the increasing demand for coal resources, the development and mining of steeply dipping coal seams have become increasingly urgent. Hence, theoretical and technical research on the mining of such coal seams holds significant practical and strategic importance.

During the mining of steeply dipping coal seams, a stress concentration zone develops at the end of the working face. The overburden is subjected to both normal loads perpendicular to the bedding planes and shear loads parallel to them, resulting in distinctive movement patterns and a more complex evolution path for the mining-induced stress transfer compared with that observed in typical coal seams [4–7]. In recent years, scholars have investigated the evolution laws of the surrounding rock in the mining of fully mechanized steeply dipping coal seams through numerical simulations, theoretical analyses, simulation experiments with similar materials, and field measurements. They have analyzed the failure zone evolution in steeply dipping working faces [8], the manifestation of ground pressure under mining influence [9], and the stability of the surrounding rock in working faces [10–12]. Due to the influence of the large dip angle, asymmetric deformation occurs in the overburden after the working face advances, leading to an increase in the internal shear stress and changes in both the magnitude and direction of the principal stress [13], ultimately resulting in the formation of new stress transfer paths [14, 15]. Existing studies have revealed the transfer and evolution paths of mining-induced stress in the overburden of steeply dipping coal seams across different dimensions, as well as the evolution mechanism of stress transfer paths based on shear stress angle analyses [16–19] and underlying strata behavior [20–22]. Although these studies have addressed the shear stress in the overburden, limited attention has been paid to the spatiotemporal evolution characteristics at the junction between the working face and the upper and lower roadways. Hence, clarifying the spatiotemporal evolution characteristics of the stress transfer at this junction is crucial for comprehensively understanding and revealing the mechanism and extent of the deformation and failure of the overburden and the evolution of stress transfer paths as the working face advances.

Taking the 35050 steeply dipping, fully mechanized coal mining face of Yiluo Coal Mine as the engineering background, this study investigated the spatiotemporal evolution characteristics of the stress transfer in the stress concentration zone at the junction between the working face and the upper and lower roadways. Using field measurement data (hydraulic support pressure) and laboratory-derived mechanical parameters as the foundation, and combined with FLAC3D numerical simulation, this study formulated principal stress characteristic quantities and analyzed the deformation and failure characteristics of the overburden at the junction to determine the characteristic values of the overburden stress. The spatiotemporal evolution characteristics of mining-induced stress transfer paths in the

overburden were further examined. The results can provide a reference for the safe and efficient mining of similar working faces.

2. Project Overview

2.1. Project Background

The 35050 working face of Yiluo Coal Mine is primarily used to exploit the No. II-1 coal seam. This working face has an elevation ranging from −90 to −158 m, and it employs a fully mechanized mining method. The working face is oriented along the dip direction, with an average dip angle of 38° and an average dip length of 100 m. The strike length varies between 712 m and 803 m, averaging at 755 m. The coal seam thickness ranges from 0.1 to 14.5 m, with an average thickness of 4.9 m, and the mining height is set to 5 m. The surrounding rock is predominantly composed of sandstone, sandy mudstone, carbonaceous mudstone, and mudstone. Table 1 summarizes the physical properties of the coal-bearing rock strata in the working face.

Table 1. Physical characteristics of the coal-bearing rock strata in the 35050 working face

Stratum	Rock type	Thickness (m)	Characteristics
Basic roof	Sandstone	35	Gray and light gray, fine-to-medium-grained feldspar quartz sandstone, with carbonaceous and muscovite fragments on the bedding plane
Immediate roof	Sandy mudstone	1.5	Grayish black sandy mudstone, with fine muscovite fragments on the bedding plane, relatively soft
Coal-bearing rock	No. II-1 coal	5	Soft texture
Immediate floor	Carbonaceous mudstone	1.2	Black carbonaceous mudstone, relatively soft, sheet-like, slippery surface, easy to break
Basic floor	Mudstone	6	Grayish black

2.2. Hydraulic Support Pressure Monitoring

The pressure data were collected through field monitoring from three representative hydraulic supports in the working face: the lower end (No. 2), the middle section (No. 45), and the upper end (No. 89), as illustrated in Figure 1. The monitoring results show that the pressure on the middle hydraulic supports remains relatively stable, ranging from 24 to 26 MPa. In contrast, the pressure on the supports near the end faces varies significantly, between 20 and 27 MPa, within 100 m ahead of the advancing working face.

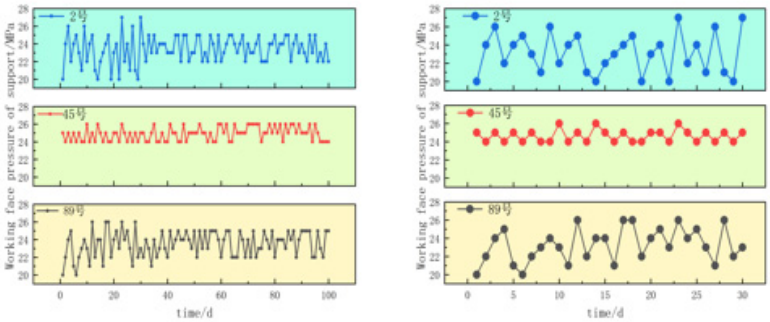

（a）Working face pressure of support （b）Excavation of 100 m support working face pressure

Figure 1. Pressure monitoring data from the working face of the support

The analysis indicates that during the advancement of the steeply dipping working face, the pressure at the ends varies considerably more than that in the middle section, with a pronounced asymmetrical distribution. This phenomenon is primarily due to changes in the surrounding rock conditions during working face mining. The stability system of a working face comprises both the hydraulic supports and the surrounding rock. In the middle section, the supports mutually interact in an effective manner, forming a relatively stable integrated system. However, at the ends, the presence of upper and lower roadways leads to a stress concentration, resulting in localized stress concentration zones. Hence, investigating the spatiotemporal evolution characteristics of the stress transfer paths at the working face ends is important for ensuring the safe and efficient mining of steeply dipping coal seams.

3. Spatiotemporal Evolution Characteristics of Stress Transfer Paths at Working Face Ends

Numerical calculation models are valued for their intuitiveness and real-time data monitoring capabilities. By constructing a numerical model, this study systematically analyzed the spatiotemporal evolution characteristics of the stresses at the working face ends during mining advancement, thereby revealing the stress transfer paths and their corresponding spatiotemporal evolution characteristics.

3.1. Numerical Calculation Model

Based on geological data of the 35050 working face of Yiluo Coal Mine and laboratory test results from field sampling, a numerical calculation model was developed using the FLAC3D software. The model dimensions were 100 m (lateral, x) × 100 m (along the coal seam strike direction, y) ×

200 m (height, z). Based on the field monitoring data (Figure 1), the first 100 m of the working face advancement represents a critical stage for stress evolution. Therefore, a 100 m section along the strike direction was selected to capture the initial characteristics of the stress concentration zone at the working face end. The dip angle of the coal seam was 38°. The model included overlying strata, a coal seam, and underlying floor strata. The model mesh comprised quadrilateral grids and hexahedral elements, totaling 2,061,266 elements and 2,078,739 nodes. The Mohr–Coulomb plastic constitutive model combined with a deformation model was employed to simulate strata deformation. The physical and mechanical parameters of each coal-bearing rock stratum were determined based on laboratory measurements of on-site samples, as summarized in Table 2. Figure 2 shows the 3D numerical model.

Table 2. Physical and mechanical parameters of coal-bearing rock strata

Name	Lithology	Thickness (m)	Density (kg·m−3)	Volume modulus (GPa)	Shear modulus (GPa)	Tensile strength (MPa)	Internal cohesion (MPa)	Internal friction angle (°)	Inclination angle (°)
Basic roof	Sandstone	35	2666.19	2.9	1.74	3.357	9.5	41	38
Immediate roof	Sandy mudstone	1.5	2751	2.91	1.5	2.601	7.8	32	38
Coal seam	Coal	5	1260.33	0.63	0.145	0.2	0.34	33	38
Immediate floor	Carbonaceous mudstone	1.2	2461	6.08	3.47	0.605	1.2	30	38
Basic floor	Mudstone	6	2567	4.3	2.8	1.68	0.7	30	38

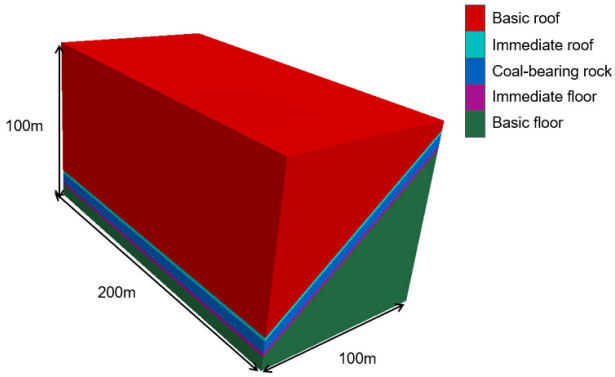

Figure 2. Numerical calculation model

The numerical simulation scheme employed in this study can be described as follows: (1) The mechanical parameters of the coal-bearing rock strata, listed in Table 2, were assigned to the corresponding model layers. All the boundaries, except for the upper surface, were fixed, and equilibrium calculations were performed. In situ stress was applied to the top and lateral sides of the model. These in situ stress parameters were based on field measurements from the 35050 working face of Yiluo Coal Mine. An equivalent stress of 6 MPa corresponds to a burial depth of approximately 200 m (1 MPa/25 m), and a lateral pressure coefficient of 1.2 aligns with the regional tectonic stress characteristics. (2) The changes at the working face end during working face advancement were simulated based on actual engineering conditions. The projected working face length was 50 m, with a mining height of 4 m, and the face advanced along the positive y-axis direction. The total advancement distance was 100 m, with an excavation step interval of 20 m. (3) Using Fish language, we performed secondary development on numerical models with varying excavation step distances to investigate the stress transfer paths in the overburden at the junction between the working face end and the upper and lower roadways.

3.2. Secondary Development of the Numerical Calculation Model

In the investigation of the stress transfer and spatiotemporal evolution characteristics within the stress concentration zone at the working face end, it is challenging to visualize the stress transfer paths and spatiotemporal evolution characteristics of the surrounding rock using a single stress component alone. To illustrate these characteristics in the stress concentration zone more intuitively, a comprehensive stress characteristic quantity was formulated based on the theory of elasticity. Subsequently, the stress data at the working face end across different stages of advancement were extracted using the Fish language, and the calculation and analysis were performed based on the stress characteristic quantity formula specific to the working face end. The detailed steps are as follows:

(1) According to the elasticity theory [23-25], the stress components at any point within a rock stratum can be denoted by σ_x, σ_y, σ_z, τ_{xy}, τ_{yx}, τ_{xz}, τ_{zx}, τ_{yz}, and τ_{zy}. Among these, τ_{xy} and τ_{yx}, τ_{xz} and τ_{zx}, and τ_{yz} and τ_{zy} are equal in magnitude, where τ_{xy}, τ_{yx}, τ_{zx}, and τ_{zy} represent the horizontal shear stresses. As illustrated in Figure 3, performing vector decomposition and synthesis on the dip profile components σ_z and τ_{zx} yields the values of the stress characteristic quantities $\sigma_{\tau x}$ of the surrounding rock, and their angles relative to the z-axis can be determined as follows:

$$\sigma_{\tau x} = \sqrt{\sigma_z^2 + \tau_{zx}^2} \tag{1}$$

$$\tan\theta_{\sigma\_\tau x} = \frac{\tau_{zx}}{\sigma_z} \tag{2}$$

Similarly, the stress characteristic quantity $\sigma_{\tau y}$ of the surrounding rock along the working face strike and its angle with the z-axis can be respectively expressed as follows:

$$\sigma_{\tau y} = \sqrt{\sigma_z^2 + \tau_{zy}^2} \tag{3}$$

$$\tan\theta_{\sigma\_\tau y} = \frac{\tau_{zy}}{\sigma_z} \tag{4}$$

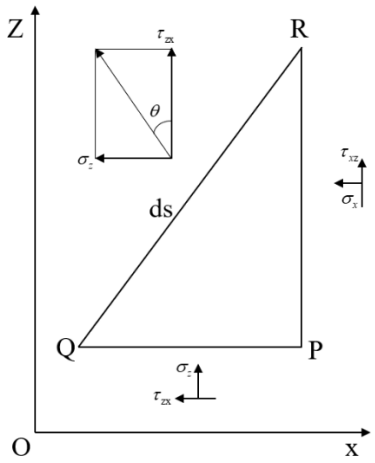

Figure 3. Analysis of the stress characteristic quantities at a certain point on the working face.

The stress characteristic quantity $\sigma_{\tau z}$ of the surrounding rock along the direction parallel to the coal seam and its angle with the z-axis can be respectively expressed as follows:

$$\sigma_{\tau z} = \sqrt{\tau_{zx}^2 + \tau_{zy}^2} \tag{5}$$

$$\tan\theta_{\sigma\_\tau z} = \frac{\tau_{zy}}{\tau_{zx}} \tag{6}$$

(2) During the excavation process of the working face, the abutment pressure plays a critical role in ensuring safe and efficient mining operations. At the working face end, due to the combined support and shielding effects provided by the hydraulic supports, the stress transfer path and surrounding rock behavior differ significantly from those in the middle section of the working face [25]. In dipping coal seams, the abutment pressure can be analyzed through the decomposition and synthesis of the stress components based on the elasticity theory, allowing for the determination of the abutment pressure on the surrounding rock. According to the elasticity theory [24], the normal stress σ_n perpendicular to the coal seam plane, the shear stress τ_{nx} along the coal seam dip, and the shear stress τ_{ny} along the coal seam strike direction can be expressed as:

$$\begin{cases} \sigma_{\mathrm{n}} = p_z\cos\alpha - p_x\sin\alpha \\ \tau_{\mathrm{nx}} = p_z\sin\alpha + p_x\cos\alpha \\ \tau_{\mathrm{ny}} = p_y \end{cases} \tag{7}$$

From the above equations, the total stresses p_x, p_y, and p_z acting on a unit can be expressed in the following matrix form:

$$\begin{bmatrix} p_x \\ p_y \\ p_z \end{bmatrix} = \begin{bmatrix} \sigma_x & \tau_{xy} & \tau_{xz} \\ \tau_{xy} & \sigma_y & \tau_{yz} \\ \tau_{xz} & \tau_{yz} & \sigma_z \end{bmatrix} \begin{bmatrix} l \\ m \\ n \end{bmatrix} \tag{8}$$

(3) In FLAC3D, the stress components, such as σ_z and τ_{zx}, within a unit can be accessed using the built-in function "z-stress" in the Fish language. Using the extracted stress data, Equations (1)–(6) can be solved simultaneously to determine the stress characteristic quantities $\sigma_{\tau x}$, $\sigma_{\tau y}$, and $\sigma_{\tau z}$ at the working face end. These values are then substituted into Equations (7) and (8) to process the stress data and identify the distribution pattern of the abutment pressure.

3.3. Evolution Characteristics of $\sigma_{\tau x}$ Along the Dip Direction

A dip measurement plane was established in the middle of the working face. Numerical calculation results obtained under different excavation step distances during the advancement of the working face were extracted and post-processed to obtain the distribution characteristics of the stress characteristic quantity $\sigma_{\tau x}$ of the surrounding rock.

The following observations can be made from the results presented in Figure 4: (1) Influenced by the coal seam dip, the transfer path of the stress characteristic quantity $\sigma_{\tau x}$ exhibits an asymmetric distribution, as illustrated in Figures 4a–e. At the lower end of the working face, the stress offset boundary line forms an "n"-shaped pattern, with the stress surrounding the junction and being transferred toward the working face. In the middle section of the working face, the boundary line is relatively smooth with minor fluctuations, and the stress transfer direction gradually shifts from the self-stress boundary line toward the working face until it becomes nearly perpendicular to it. At the upper end of the working face, the boundary line takes a convergent, arch-shaped form. A stress-surrounding phenomenon similar to that observed at the lower end occurs at the junction, with the stress being transferred toward the working face. (2) As shown in Figure 4f, the stress offset boundary line of the overlying strata gradually expands outward with increasing advancement distances, forming an overall "m"-shaped pattern. The arch soffits are located at the junctions between the upper and lower ends of the working face, while the left and right arch tops are approximately aligned with the positions perpendicular to the central axis of the working face at these junctions. The arch feet are located at the upper and lower ends of the working face. Within the arch, the stress transfer direction shows a significant deflection, gradually aligning in a direction perpendicular to the working face in the middle section. At the upper and lower ends, the stress gradually transfers upward and downward toward the working face. Outside the stress arch, the deflection amplitude is relatively low, with the stress primarily being transferred vertically downward. (3) Referring to Figure 4f again, the stress offset boundary line of the underlying strata is overall arch-shaped, with the curvature increasing with the advancement distance. The evolution pattern transitions from an initial wrapping shape around the working face underlying the strata at an advancement of 20 m to a more encompassing configuration surrounding the working face underlying strata, with the stress offset boundary line extending accordingly. Within the stress arch, the stress transfer direction shows a significant deflection. At the upper and lower ends, the stress gradually shifts toward the center of the working face from distant to near positions, while in the middle section, the direction remains perpendicular to the working face. Outside the stress arch, due to the overall change in the transfer direction, a

behavior different from that observed in the overlying strata is seen, with the stress deflection amplitude increasing with decreasing distance from the stress arch. (4) As the working face advances further, the asymmetry in the stress characteristic quantity $\sigma_{\tau x}$ in the overlying strata becomes increasingly pronounced, and the extent of the stress arch continues to expand. The projection of the arch top onto the x-axis gradually shifts to the left, indicating an increasing distance from the vertical central axis of the working face. However, it remains relatively aligned with the axis perpendicular to the working face. Moreover, the vertical distance between the arch top and the working face shows a progressively increasing trend.

The distribution pattern and deflection direction of the stress characteristic quantity $\sigma_{\tau x}$ determine the stress transfer behavior, which in turn influences the loading characteristics at the junctions between the upper and lower ends of the working face. To investigate the evolution characteristics of the abutment pressure at these junctions, a measurement line was established at the central position of the junctions, and the abutment pressure data from the coal body along the working face were extracted. Figure 5 shows the results. As shown, the dipping strata cause the abutment pressure at the lower end of the working face to be higher than that at the upper end. With the advancement of the working face, the extent of the stress offset boundary line gradually expands, and the overburden load is transferred to the undisturbed zone, ultimately increasing both the stress offset region and the abutment pressure.

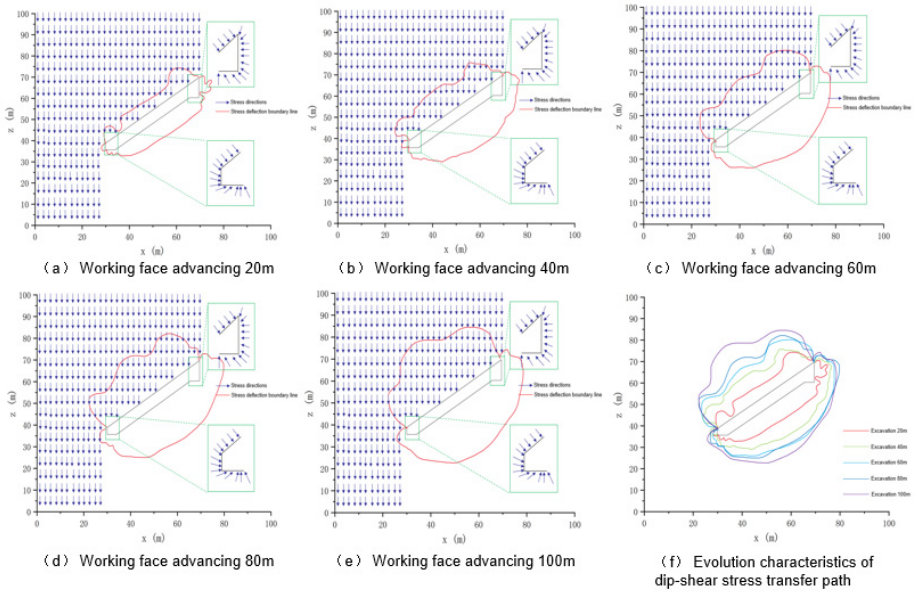

Figure 4. Evolution of the stress $\sigma_{\tau x}$ in the overburden along the working face dip direction.

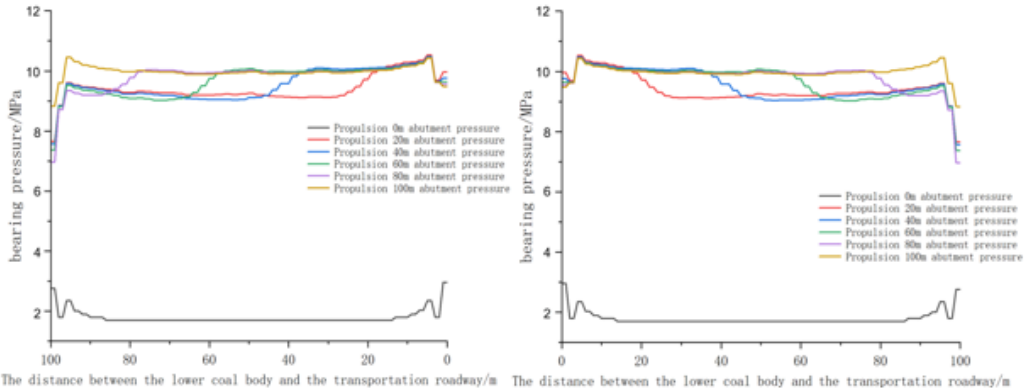

Figure 5. Evolution of the abutment pressure along the dip direction.

3.4. Evolution Characteristics of $\sigma_{\tau y}$ Along the Strike Direction

A strike measurement plane was established at the junctions between the upper and lower ends of the working face. Numerical calculation results obtained under different excavation step distances during the advancement of the working face were extracted and post-processed to obtain the distribution characteristics of the stress characteristic quantity $\sigma_{\tau y}$ of the surrounding rock.

The following observations can be made from Figures 6 and 7: (1) The stress characteristic quantity $\sigma_{\tau y}$ of the overlying strata at the upper end of the working face exhibits an asymmetric distribution. The stress offset boundary line forms an asymmetric “m”-shaped stress arch, with the advancing position as the center. As the working face advances, the stress offset boundary line gradually becomes symmetrical with respect to the central axis of the working face. The load of the overlying strata on both sides of the symmetry axis is directed toward the coal bodies on either

side of the working face, resulting in an arch-shaped distribution of the $\sigma_{\tau y}$ transfer path. Within the arch, the transfer path of $\sigma_{\tau y}$ gradually tilts toward the start-up cut direction from the working face position, while near the goaf, the transfer path of $\sigma_{\tau y}$ shifts slightly toward both ends. The stress offset at the stress offset boundary line approaches zero. (2) The stress characteristic quantity $\sigma_{\tau y}$ of the underlying strata at the upper end of the working face also shows an asymmetric distribution. The stress offset boundary line forms a "U"-shaped pattern, with the central axis of the advancing position serving as the symmetry axis. As the working face advances, the symmetry axis gradually aligns with the central axis of the working face. The load of the underlying strata on both sides of the symmetry axis is again directed toward the adjacent coal bodies, resulting in an arch-shaped distribution of the $\sigma_{\tau y}$ transfer path. Within the arch, the transfer path of $\sigma_{\tau y}$ gradually shifts toward the working face position until it becomes nearly perpendicular to the working face direction, with only minor deviations. Due to the dominant transfer direction of $\sigma_{\tau y}$ of the underlying strata in the positive z-axis, the stress offset at the stress offset boundary line remains clearly visible. (3) The distribution pattern of the stress characteristic quantity $\sigma_{\tau y}$ in the overlying strata at the lower end of the working face is generally similar to that of the stress characteristic quantity $\sigma_{\tau y}$ in the overlying strata at the upper end of the working face. However, the stress arch formed by the stress offset boundary line is slightly smaller than that at the upper end. Furthermore, as the working face advances, the stress transfer path at the start-up cut and working face position shifts toward the undisturbed zone and converges near the lower floor, eventually aligning with the negative z-axis direction. (4) The stress characteristic quantity $\sigma_{\tau y}$ of the underlying strata at the lower end of the working face does not exhibit a distinct stress arch phenomenon. As the working face advances, the stress boundary line remains close to the floor of the working face, and the stress transfer path is primarily perpendicular to the floor, with slight deviations toward the adjacent coal bodies on both sides of the working face. (5) The extent of the stress arch increases continuously with the advancement distance of the working face. The deflection angle of $\sigma_{\tau y}$ within the arch also increases with the distance from the working face position, reaching its maximum at the working face itself. Outside the stress arch, the deflection angle of $\sigma_{\tau y}$ closely aligns with the negative z-axis direction, with no significant offset observed. (6) The transfer paths and stress boundary line ranges of the stress characteristic quantity $\sigma_{\tau y}$ differ between the upper and lower ends of the working face. For the overlying strata, the stress arch range at the lower end is significantly narrower than that at the upper end, and the internal stress transfer paths also differ. At the lower end, the stress transfer path is primarily directed toward the start-up cut, rather than exhibiting the symmetrical offset seen at the upper end. This deviation is attributed to the influence of the dipping strata, which restrict the stress transfer at the lower end more than that at the upper end.

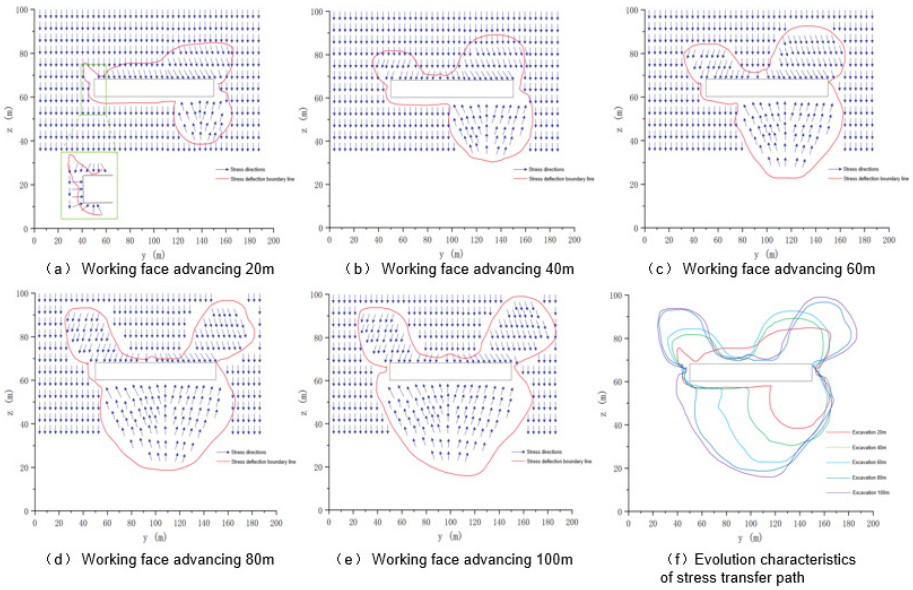

Figure 6. Evolution characteristic of the overburden stress $\sigma_{\tau y}$ at different advancement distances of the upper end of the working face along the strike direction.

3.5. Evolution Characteristics of $\sigma_{\tau z}$ Along the Dip Direction

Based on the aforementioned analysis, the transfer and evolution patterns of the stress characteristic quantities along both the dip and strike directions of the steeply dipping coal seam have been identified. However, the specific stress transfer paths at the junction of the upper end at different positions remain unclear. To address this, numerical simulation results at an advancement distance of 100 m were extracted along a cross-section parallel to the coal seam, and the stress characteristic quantities from different layers were analyzed.

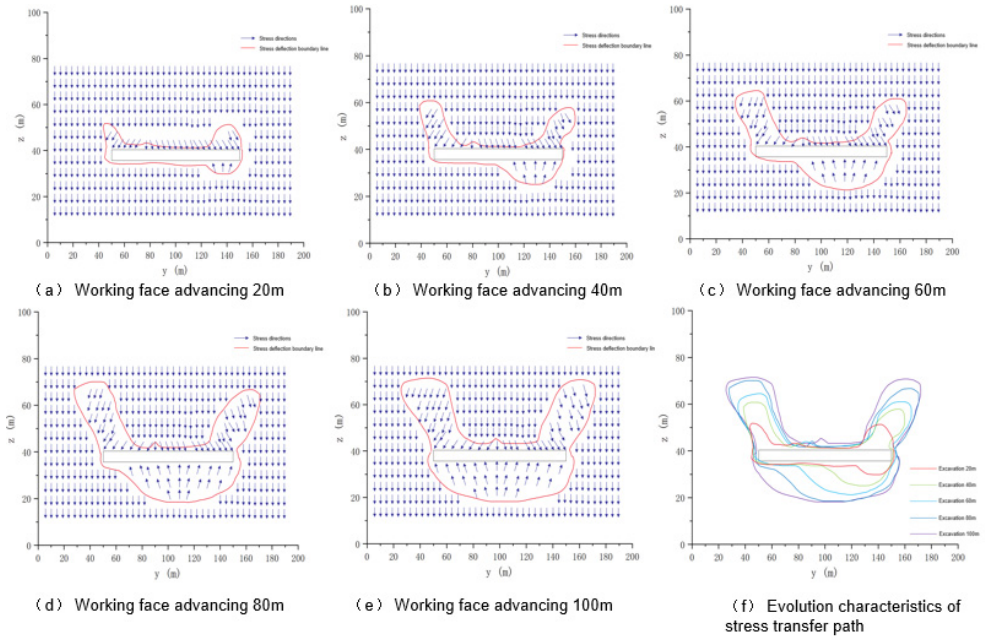

Figure 7. Evolution characteristic of the overburden stress $\sigma_{\tau y}$ at different advancement distances of the lower end of the working face along the strike direction

Figures 8 and 9 show the processed results, where the x- and y-axes represent the dip and strike directions of the working face, respectively. As shown in Figure 8, the stress characteristic quantities $\sigma_{\tau z}$ of the roof and floor exhibit an asymmetric distribution along the dip direction and a symmetric distribution along the strike direction due to the influence of the coal seam dip angle. The transfer and evolution characteristics of the roof and floor stress characteristic quantities $\sigma_{\tau z}$ at the end position of the working face are summarized as follows: (1) The stress offset boundary line is symmetrically distributed, with the strike centerline of the coal seam as the axis of symmetry. As the distance from each layer increases, the boundary line gradually approaches the projected center point of the working face. The zero position of the roof shear stress τ_{xz} is defined as the boundary line of the roof shear stress τ_{xz}, with the stress transfer paths of the surrounding rock on either side directing toward both sides of the working face. The offset angle of the stress characteristic quantities $\sigma_{\tau z}$ increases with increasing distance from the boundary line. The position of the boundary line of the shear stress τ_{xz} shifts slightly with increasing distance from the coal seam until it aligns with the dip centerline of the coal seam. Within the projected range of the goaf, the transfer direction of the stress characteristic quantities $\sigma_{\tau z}$ is inclined toward both sides along the dip direction in the middle section of the goaf and toward the boundary positions at the start-up cut and working face. Outside the goaf range, the stress characteristic quantities $\sigma_{\tau z}$ on the left side tend to cluster around the goaf, while the stress characteristic quantities $\sigma_{\tau z}$ on the right side propagate unidirectionally along the strike direction of the working face, in the positive x-axis direction. The transfer paths of the stress characteristic quantities $\sigma_{\tau z}$ along both sides of the y-axis outside the goaf are similar to those in the adjacent regions within the goaf, with the offset direction nearly aligned along the boundary toward the coal seam. (2) The transfer path of the stress characteristic quantities $\sigma_{\tau z}$ at the floor position resembles that on the roof, with the zero position of the roof shear stress τ_{xz} serving as the boundary line of the roof shear stress τ_{xz}. On both sides of the boundary line, the stress transfer paths of the surrounding rock are directed toward both sides of the working face, and the offset angle of the stress characteristic quantities $\sigma_{\tau z}$ increases with increasing distance from the boundary line. The key difference is that the symmetry axis of the stress deflection boundary line is shifted downward slightly.

In conclusion, the stress transfer and evolution characteristics of the overburden at the end of a working face in a steeply dipping coal seam are significantly more complex than those observed in the middle of the working face or in general coal seams. Influenced by the coal seam dip angle, the overburden stress exhibits an asymmetric distribution along the dip direction and a symmetric distribution along the strike direction. Furthermore, the spatial structural distribution and evolution patterns of the overburden under different advancement distances of the working face are largely consistent.

4. Conclusion

This study revealed, for the first time, the “stability–fracture” periodic evolution law of the stress arch formed at the junction between the working face and the upper and lower roadways in steeply dipping coal seams, effectively addressing the limitations of previous studies that focused solely on either the roof or floor strata.

(1) Influenced by the dip angle of the coal seam, the support pressure exhibited regional characteristics. The pressure distribution in the middle section of the working face was relatively stable and uniform, whereas the pressure at the end

regions showed significant dispersion.

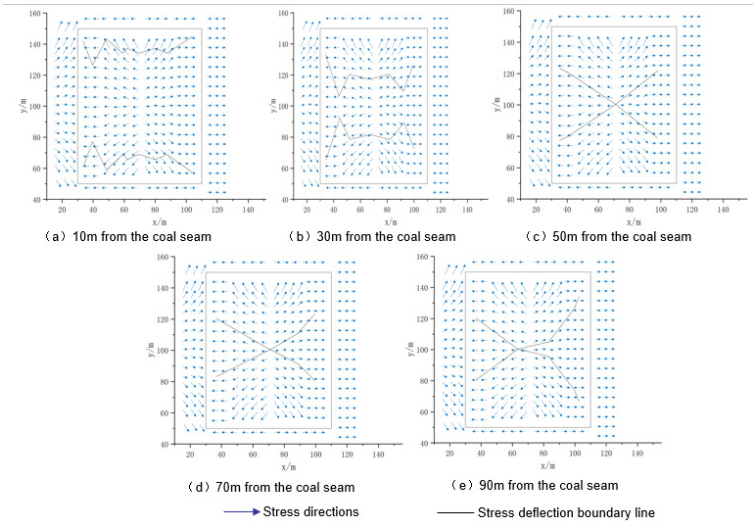

Figure 8. Evolution characteristics of the stress $\sigma_{\tau z}$ parallel to the coal seam in roof strata at different levels.

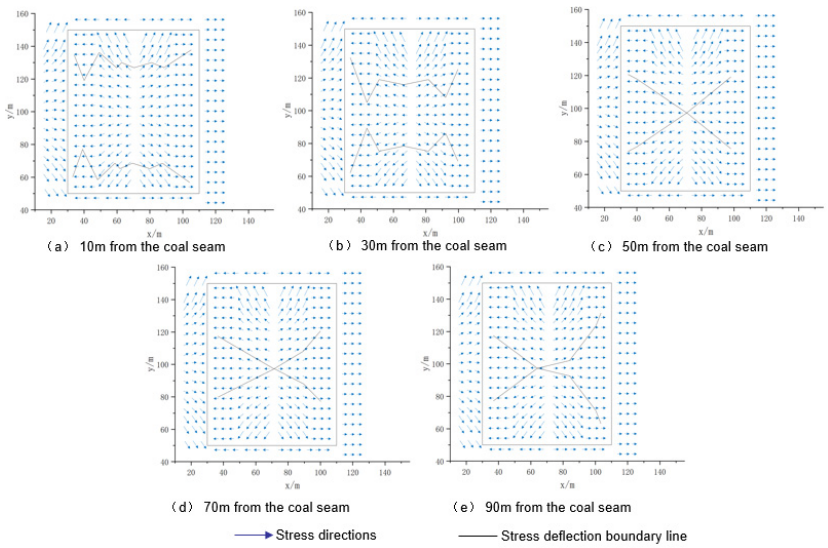

Figure 9. Evolution characteristics of the stress $\sigma_{\tau z}$ parallel to the coal seam in floor strata at different levels.

(2) Along the strike direction of the working face, the stress deflection boundary of the roof at the junction of the working face end formed an “n”-shaped arch. The stress arch range at the lower end was wider than that at the upper end, consistent with the stress distribution characteristics of dipping strata. As the working face advanced, the range of the stress deflection boundary gradually widened. The floor stress deflection boundary exhibited a wrapped morphology, and its range and arch height variation trend were consistent with those of the roof.

(3) In the strike direction, the roof stress boundary line at the junction of the working face end was significantly more confined at the lower end than at the upper end, forming an asymmetric “m”-shaped arch. The boundary range at the junction was notably wider compared with that at the opposite side. As the working face advanced, the roof stress boundary line evolved into a double “n”-shaped arch, with the start-up cut and the working face as the apexes. This evolution was attributed to the uneven stress release on both sides of the goaf, and the range of the stress boundary line showed a progressively increasing trend.

(4) In the direction parallel to the coal seam, the stress boundary lines of the goaf and roof collectively exhibited an asymmetric arch-shaped distribution. The stress arch range at the lower end was significantly wider than that at the upper end, and with increasing distance from the coal seam, the boundary line gradually approached the strike centerline of the coal seam. When the boundary line was approximately 90 m away from the coal seam, it evolved into a “V”-shaped structure with the strike centerline as the symmetry axis, forming an angle of approximately 60°, which correlated with the higher stress concentration at the lower end. The stress boundary line behavior of the floor was similar to that of the roof, with the exception that the symmetry axis of the stress deflection boundary line shifted slightly downward.

References

[1] H.P. Kang, Seventy years development and prospects of strata control technologies for coal mine roadways in China, Chin. J. Rock Mech. Eng. 40 (2021) 1–30.

[2] X. Song, D. Zhu, Z. Wang, Y. Huo, Y. Liu, G. Liu, J. Cao, H. Li, Advances on longwall fully-mechanized top-coal caving mining technology in China during past 40 years: theory, equipment and approach, Coal Sci. Technol. 49 (2021) 1–29. https://dx.doi.org/10.13199/j.cnki.cst.2021.03.001.

[3] Y. Wu, D. Lang, D. Yun, P. Xie, H. Wang, X. Gao, S. Luo, Y. Zeng, W. Lyu, Y. Zhang, B. Hu, Reform and prospects of mining technology for large inclined coal seam in China, Coal Sci. Technol. 52 (2024) 25–51. https://dx.doi. org/10. 12438/ cst.2023-1601.

[4] Y. Wu, P. Xie, S. Ren, Analysis of asymmetric structure around coal face of steeply dipping seam mining, J. China Coal Soc. 35 (2010) 182–184.

[5] Y. Wu, D. Lang, X. Panshi, Mechanism of disaster due to rib spalling at fully-mechanized top coal caving face in soft steeply dipping seam, J. China Coal Soc. 41 (2016) 1878–1884.

[6] Y. Wu, W. Liu, P. Xie, S. Tian, Stress evolution and roof breaking characteristics of surrounding rock in oblique longwall mining area of steeply dipping seam, Saf. Coal Mines. 51 (2020) 222–227.

[7] Y. Wu, P. Xie, D. Yun, H. Wang, S. Luo, X. Gao, D. Lang, B. Hu, Z. Yan, T. Wang, Gravity-dip effect and strata control in mining of the steeply dipping coal seam, J. China Coal Soc. 48 (2023) 100–113.

[8] J.A. Wang, J.W. Zhang, X. Gao, J.D. Wen, Y.D. Gu, Fracture mode and evolution of main roof stratum above fully mechanized top coal caving longwall coalface in steeply inclined thick coal seam (II): Periodic fracture, J. China Coal Soc. 40 (2015) 1737–1745.

[9] T. Long, L. Xun, T. Hongsheng, W.A. Lei, S.U. Maoru, Z.H. Jicheng, C.A. Dibiao, M.A. Shoulong, Study on mine pressure law of compound roof working face with large dip angle under the influence of mining, Coal Sci. Technol. 50 (2022) 58–66.

[10] Z. Wang, Y. Liang, Q. Zou, B. Zhang, Q. Ran, Movement of overlying rock and deformation law of surface well under multiple mining with large dip angle, Coal Sci. Technol. 51 (2023) 47–55. https://dx.doi.org/10.13199/j.cnki.cst.2021-0827.

[11] W. Cao, H. Liu, Y. Hang, H. Wang, G. Li, Similarity simulation on the movement characteristics of surrounding rock and floor stress distribution for large-dip coal seam, Sensors (Basel). 22 (2022) 2761. https://doi.org/10. 3390/ s22 072761.

[12] H. Shaoxuan, M. Liqiang, G. Jinshuai, Y. Peiju, Support-surrounding rock relationship and top-coal movement laws in large dip angle fully-mechanized caving face, Int. J. Min. Sci. Technol. 28 (2018) 533–539. https://doi.org/10.1016/j. ijmst. 2017.10.001.

[13] K. Zhu, Z. Li, S. Luo, P. Xie, J. Fan, T. Wang, C. Tian, Z. Yan, Spatiotemporal evolutionary characteristics of asymmetric stress transfer in overburden of steeply dipping coal seams, Coal Geol. Explor. 52 (2024) 129–140. https://doi.org/ 10. 12363/ issn.1001-1986.24.06.0392.

[14] Y. Zhao, J. Yu, C. Zhou, K. Zhao, H. Xiao, Characterization of pressure arching effect of arch shell surrounding rock considering deviation of principal stress axis, Chin. J. Geotech. Eng. 43 (2021) 1842–1850.

[15] B. Huang, P. Xie, Y. Wu, W. Lin, S. Luo, S. Wang, Z. Wen, J. Chen, The effect of overlying rock fracture and stress path evolution in steeply dipping and large mining height stope, Geomech. Geophys. Geo Energ. Geo Resour. 10 (2024) 95. https://doi.org/10.1007/s40948-024-00803-8.

[16] K. Yang, Z. Wei, X. Chi, A. Gao, Q. Fu, Fracture criterion of basic roof deformation in fully mechanized mining with large dip angle, Energy Explor. Exploit. 39 (2021) 886–902. https:// doi. org/10.1177/0144598720986628.

[17] H. Wang, Y. Wu, M. Liu, J. Jiao, S. Luo, Roof-breaking mechanism and stress-evolution characteristics in partial backfill mining of steeply inclined seams, Geomat. Nat. Haz. Risk 11 (2020) 2006–2035. https://doi.org/10. 1080/ 19475 705. 2020.1823491.

[18] P. Xie, B. Huang, Y. Wu, S. Luo, T. Wang, Z. Yan, J. Chen, Dip-angle-effect-based deformation and failure law of steeply dipping stope roofs with large mining heights, Arch. Min. Sci. 68 (2023) 507–524. https://doi.org/10.24425/ams.2023.146865.

[19] B. Hu, P. Xie, B. Huang, Y. Wu, J. Chen, Study on roof breaking mechanism and support stability of steeply dipping seam and large mining height, Energy Explor. Exploit. 42 (2024) 544–566. https://doi.org/10.1177/01445987231203464.

[20] Y. Chen, Z. Wang, Q. Hui, Z. Zhu, D. Sun, Y. Chen, X. Zhang, Z. Wang, J. Wang, J. Zhao, Overlying rock movement and mining pressure in a fully mechanized caving face with a large dip angle, Front. Earth Sci. 10 (2022) 963973. https://doi.org/ 10. 3389/feart.2022.963973.

[21] S. Luo, Y. Wu, H. Wang, P. Xie, Asymmetric failure pattern and slip characteristics of floor of longwall face in steeply dipping seam mining, J. China Coal Soc. 43 (2018) 2155–2161. https://dx.doi.org/10.13225/j.cnki.jccs.2018.0144.

[22] A.J. Das, P.K. Mandal, R. Bhattacharjee, S. Tiwari, A. Kushwaha, L.B. Roy, Evaluation of stability of underground workings for exploitation of an inclined coal seam by the ubiquitous joint model, Int. J. Rock Mech. Min. Sci. 93 (2017) 101–114. https://doi.org/10.1016/j.ijrmms.2017.01.012.

[23] Z. Xu, Elasticity, People's Education Press, 1979.

[24] X. Xian et al., Failure Mechanism of Stratified Rock Mass., Chongqing University Press, 1989.

[25] M. Qian et al., Mining, Ground Press. Strata Control, China University of Mining and Technology Press (2010).